1 # MR relaxometry-based analysis of brain hemorrhages: an

2 # experimental study on a rabbit model

3

4 ## MR Relaxometry and brain hemorrhages

5

6 **Francesca Del Signore[1], Massimo Vignoli[1], Leonardo Della Salda[1*], Roberto Tamburro[1],**

7 **Ilaria Cerasoli[2], Andrea Paolini[1], Mariarita Romanucci[1], Francesco de Pasquale[1].**

8

9 **[1] Veterinary Faculty, University of Teramo, Teramo, Italy**

10 **[2]Clinica Veterinaria Borghesiana, Rome, Italy**

11

12 **[*]Corresponding author**

13 **Email: ldellasalda@unite.it (LDS)**

14

15

16

17

18

19

20

21

22

23

24

Abstract

Magnetic Resonance Relaxometry is a quantitative MRI-based technique able to estimate tissue relaxation times T1 and T2. This approach allows increasing the MRI diagnostic accuracy mostly in case of brain neoplasia or neurodegenerative disorders in human medicine. However, few reports are available on the application of this technique in the clinical field of veterinary medicine. For this reason, in this work, we developed a relaxometry based approach on experimentally induced brain hemorrhages on rabbits. Specifically, the methodology is based on a hierarchical clustering procedure driven by the T1 relaxometry signals from a set of regions of interest selected on the T2 map. The approach is multivariate since it combines both T1 and T2 information and allows the diagnosis at the subject level by comparing "suspected" pathological regions with healthy homologous ones within the same brain.

To validate the proposed technique, the scanned brains underwent histopathological analyses to estimate the performance of the proposed classifier in terms of Receiver Operator Curve analyses. The results showed that, in terms of identification of the lesion and its contours, the proposed approach resulted accurate and outperformed the standard techniques based on T1w and T2w images. Finally, since the proposed protocol in terms of the adopted scanner, sequences, and analysis tools, is suitable for the clinical practice, it can be potentially validated through large-scale multi-center clinical studies.

Introduction

44

45 Magnetic Resonance Imaging (MRI) is considered the gold standard imaging technique to investigate

46 encephalic disorders in companion animals [1,2]. However, the images' evaluation is typically

47 qualitative since MRI provides signals only weighted on the actual tissue longitudinal (T1) and

48 transverse (T2) relaxation times. To overcome this limitation and to obtain more objective

49 information on the structure and function of the tissues under investigation, it has been developed a

50 technique called MR-Relaxometry (MRR) able to provide maps of the actual T1 and T2 [3,4].

51 Although the intricate relationships linking the tissue microstructure to these relaxation times remain

52 to be firmly established, their quantitative measurement can be informative of disease-related tissue

53 change, developmental plasticity, and other biological processes. Therefore, MRR studies potentially

54 offer a more detailed tissue characterization as compared to conventional ones [3,4].

55 In human medicine, the MRR role has been thoroughly investigated, for example in brain neoplasia,

56 where this technique improved the lesion identification, especially when monitoring the

57 chemotherapy response [5–9]. Many reports are also available on the application of this technique on

58 epileptic patients, with the result of optimizing and enhancing lesion depiction [10,11,11–15]. In the

59 case of neurodegenerative disorders, MRR resulted useful to improve the detection of early

60 degeneration areas [16–18]. Additional examples and a general review of this technique can be found

61 in [3,4].

62 As far as it concerns Relaxometry applications on animal models, most studies have been performed

63 on rats, mainly on neoplasia [6,19,20]. Further, MRR has been useful in characterizing the

64 hippocampal involvement in epileptic patients [21] and to detect spontaneous brain hemorrhages [22].

65 However, most of the animal studies lack an accurate histopathological validation and are typically

66 performed with high field scanners characterized by a high spatial and signal-to-noise-ratio (SNR)

67 [21]. On the one hand, this allows us to achieve a higher spatial resolution and signal-to-noise ratio

68 (SNR). On the other hand, translating such protocols in the clinical field might not be straightforward

3

69   since nowadays, mainly low field scanners, characterized by a low spatial resolution and SNR, are

70   available in veterinary facilities [23]. Typically, the diagnosis is based on standard T1w/T2w images

71   and small lesions can be missed. Further, it often strongly relies on the radiologist's experience, e.g.

72   in case of subtle lesions, hepatic encephalopathy, distemper encephalitis, or small hemorrhages

73   [24,25]. To overcome these limitations, in the clinical field, an advanced MRR based tool, as long as

74   compatible with a low field scanner equipment, could be helpful, as shown in [22]. In this preliminary

75   study, we showed the potentiality of a relaxometry protocol implemented on a 0.25 T scanner and

76   tested on phantom and real data from a healthy dog [22]. Here, we built upon those results to focus

77   on experimentally induced hemorrhages on rabbit brains. This model allows to work with brains

78   whose size is similar to canine and feline species so that the developed protocol might be translated

79   to these species. Further, smaller brain animals were excluded due to the resulting prohibitive SNR

80   of the adopted MR scanner.

81   The developed approach can be summarized as follows. First, a set of regions of interest were selected

82   based on a T2 map. Second, a hierarchical clustering, driven by the T1 relaxation patterns of the

83   selected regions, compared the selected regions with the healthy homologous ones and classified the

84   tissues under investigation. Finally, the performance of the proposed classifier was assessed through

85   the comparison with histopathological examinations of the brains under investigation.

86

Materials and methods

Cerebral hemorrhage model in rabbits

Sixteen New Zealand White male rabbits (*O. Cuniculus*) (3.2 ± 0.5 kg) were included in this study, that has been carried out in strict accordance with the recommendation from national committee for animal welfare, with the procol N° 726/2019-PR; all the subjects received continuous proper care according to national guidelines under the supervision of trained personal.

Eight hours before the procedure, each rabbit received meloxicam (1,5 mg kg -1) (Metacam, 1,5 mg/ml, Boehringer Ingelheim Div. Veter) intramuscular (IM) to obtain multimodal analgesia integrated with morphine (1 mg kg -1) (morphine chloride, 10 mg/mL, S.A.L.F. S.p.a) and midazolam (0,5 mg kg -1) (Dormicum®, 5 mg/ml, Roche Pharma, Switzerland) for IM premedication before the start of the procedure. Sixty minutes before applying auricular venous and arterial catheter (22 -24 G 2,5 cm) to properly administer fluids and drugs as needed, and measure blood pressure respectively, each rabbit received topic administration of EMLA cream 5% ® (Aspen Pharma Trading Limited). Induction has been performed with alfaxalone (1-4 mg kg -1) (Alfaxan®, 10 mg/ml, Jurox, UK) intravenous (IV) and general anesthesia was maintained with isoflurane in oxygen 100% after applying a cuffed orotracheal tube (2-3-5 mm ID) under endoscopic guidance.

The rabbit cerebral hemorrhaged model was established by autologous blood injection method, with 0.15 ml of blood extracted from the auricular vein. The rabbit was placed in sternal recumbency; a 1.5 cm midline sagittal skin incision was performed with a #10 scalpel blade and the subcutaneous tissue was dissected to visualize the brain "cross stitch" intersection that was set as the starting point. A 2.0 mm bone defect was manually performed on the left calvarium with a Synthes-Colibrì 2 surgical drill using a Synthes drill bit diameter 2.0 mm. The drilling starting point was 3-5 mm to the left of the coronal suture and caudal to the sagittal suture [26] (Fig 1). The drilling was perpendicularly oriented to the parietal bone surface. A stopper was applied 4 mm below the tip of the drill bit to

112   avoid any potential brain damage. Then the blood was manually injected into the left hemisphere of

113   each subject with a 1 ml syringe and a 25 G- 1.6 cm needle perpendicularly oriented to the parietal

114   bone surface to compare the two hemispheres in the same acquisition.

115

116   **Fig 1. Technical procedure to induce hemorrhages**

117   A) The brain "cross stitch" used as an anatomic landmark (black arrow).

118   B) The 2-mm diameter hole performed with a surgical drill 3-5 mm caudally and on the left of

119   the coronal suture.

120   C) The final location to inject the autologous blood and induce the cerebral hemorrhage.

121

122   Then the rabbit was carefully moved to the MR scanner. After the MR acquisitions, each subject has

123   been euthanized according to national guidelines, and brains were promptly fixed in 10% neutral

124   buffered formalin for histopathological investigations (see below).

125

MRI acquisition and relaxometry protocol

127   Thirteen out of sixteen subjects were included in the study since three rabbits died.

128   MR data were acquired using an Esaote Vetscan Grande scanner operating at 0.25 T equipped with a

129   Coil 4 (Esaote S.PA, Genova, Italy). The conventional data consisted of Spin Echo (SE) T1w and

130   Fast SE T2w sequences on transverse and sagittal planes, see Table 1 for the adopted parameters.

131

132

133

134

135

136

137

138   **Table 1. MRI acquisition parameters**

139

	T1w Transverse	T2w Transverse	T2w Sagittal
TR	400 ms	2660 ms	2170 ms
TE	18 ms	100 ms	100 ms
Slice thickness	3 mm	3 mm	3 mm
Gap	0 mm	0 mm	0 mm

140

141   Settings for T1w -T2 w transverse and T2 w sagittal sequences.

142

143   Based on these acquired images, a single transverse brain slice was selected to perform both T1 and

144   T2 relaxometry. This slice was selected to contain the suspected localization of the lesion in the

145   transverse plane. When the lesion was not clearly identifiable in this plane, sagittal sequences were

146   used to localize the lesion.

147   T1 Relaxometry data were acquired through an ad-hoc protocol based on repeated acquisitions of SE

148   T1w images corresponding to a variable TR, namely TR = [50 120 200 300 400 500 600 650 750 850

149   900 950 1000] ms. This set of values has been optimized in a previous study [22]. As far as it regards

150   T2 relaxometry data these were obtained by acquiring FSE T2w images repeatedly acquired with a

151   variable TE, namely TE = [28 75 136] ms.

152   To account for small head movements during the acquisition, all the acquired images were co-

153   registered to the T1w ones, through an affine transformation using a standard approach, see for

154   example [27]. For this reason, in what follows all the acquired images and related results, such as

155   T1/T2 maps and clustering results, will result aligned in the same subject space.

156   The complete acquisition procedure lasted about 45 minutes on every subject.

7

Analysis pipeline

157
158 The proposed approach consists of a multivariate classification procedure that combines both the

159 information from T1 and T2 relaxation times. The analysis pipeline is schematized in S1 Fig.

160

Estimation of T1 and T2 maps

161
162 To estimate T1/T2 maps the acquired MR signals were fitted through a two-parameter model using

163 an unconstrained minimization algorithm based on a derivative-free method [28,29]. Then, for each

164 patient, from the obtained T2 maps a set of *n* voxels, representing ROIs of suspected lesions, were

165 manually selected by an expert radiologist (S1A Fig). The value of *n* was variable depending on the

166 extension of the suspected lesion. Then, based on the location of the brain midline, the algorithm, in

167 the contralateral hemisphere, automatically extracted additional *n* voxels corresponding regions

168 homologous to the ones selected (S1A Fig). The set of *2n* voxels will represent the input of the

169 classification algorithm. This allowed us to compare the selected ROIs with their homolog ones to

170 obtain subject-specific results avoiding the normalization into an average-based brain template.

171

Hierarchical clustering

172
173 To detect the hemorrhagic vs healthy tissues a hierarchical clustering, driven by the T1 relaxometry

174 patterns (S1B Fig), was employed (S1C Fig). Other possible clustering techniques could have been

175 adopted, but the hierarchical clustering has the advantage, e.g. as compared to K-means clustering,

176 that the number of classes does not need to be specified in advance and the progression of the

177 clustering can be evaluated at different levels.

178 The basic idea is that hemorrhagic tissues will exhibit a different pattern of relaxometry as compared

179 to healthy ones. At this stage, we decided to use the original relaxometry pattern for every voxel and

180 not the relaxation times at the previous steps. This makes the classification more robust since it

181 depends on 13 points (the number of TR adopted), and not just 1 as in the case of relaxation time,

182 thus describing more accurately the return of the MR signal to the baseline.

183 Specifically, the hierarchical clustering was run with the Euclidean distance and an unweighted

184 average as linkage criterion. The final output of the hierarchical clustering is a dendrogram showing

185 the hierarchical evolution from a set of completely separated observations to the final single cluster,

186 (S1C Fig). At this stage, to choose the optimal number of clusters, for every output, we computed the

187 cluster silhouette [30] Of note, for all the considered rabbits in this study, we obtained the highest

188 silhouette corresponding to two classes, i.e. a binary classification. Thus, in what follows, the cluster

189 of voxels whose majority was in the healthy hemisphere was labeled as "healthy" (H) while the other

190 cluster as "pathological" (P). Of note, the healthy hemisphere will always be the right one since we

191 induced hemorrhages only in the left hemisphere.

192 All the reported analyses were performed through in-house developed codes in MATLAB (MATLAB

193 and Statistics Toolbox Release 2015b, The MathWorks, Inc., Natick, Massachusetts, USA).

194

Histopathological examination

196 Brains were cut with a small guillotine specifically prepared for the experiment (see Fig 2). Each

197 brain has been positioned on a home-made wooden wedge to respect the same brain angle inclination

198 measured from MRI images during the scan protocol; this aspect has been carefully considered to

199 orient the cut parallel to the induced lesion (Fig 2).

200

201 **Fig 2. Operative procedure for brain cuts**

202   A) The inclination of the brain obtained from the T2w sagittal images.

203   B) The same inclination as in A) has been reproduced with wooden wedges to be used with a

204   small guillotine specifically prepared for the experiment.

205

206   Transverse serial sections of all fixed brains were also obtained and photographed. Then, formalin-

207   fixed paraffin-embedded brain sections (i.e, tissue blocks from all induced hematoma areas, as well

208   as from ipsilateral and/or contralateral nervous tissues, particularly frontal Cerebral Cortex, Corpus

209   Callosum, and Caudate Nucleus) were routinely processed for histology and stained with

210   hematoxylin-eosin (H&E). The acquisition of the histological images and the evaluation of the

211   margins of the lesions were carried out using the image analysis software LAS X Measurements

212   (Leica microsystem).

213

Validation of the proposed approach with histopathological analyses

215   To validate the proposed approach, the classification results were compared to the histopathological

216   findings as follows.

217   The classifier performance was assessed through a Receiver Operator Curve analyses where the

218   'ground truth' was represented by the histopathological results (S1D Fig) First, based on the

219   histological analyses, the contours of the tissues involved with the hemorrhages were extracted. In

220   what follows, we will denote this contour as the "true lesion contour". Then, these images were

221   manually co-registered to the anatomical MRI images by an expert radiologist. In this way, for every

222   rabbit, we could directly compare the classification with the ground truth. This allowed to compute,

223   for every lesion, the true positives (TP), as the number of voxels correctly classified as pathological

224   (red voxels in the figures), i.e. voxels falling within the "true lesion contour"; the false negatives

225   (FN), as the number of voxels classified as healthy falling inside the "true lesion contour"; the false

226   positives (FP), as the number of voxels classified as pathological that fell outside the "true lesion

227   contour" and the true negatives (TN) as the number of voxels classified as healthy (yellow in the

228   figures) falling outside the "true lesion contour". This allows computing the accuracy, true positive

229   rate (TPR), and false-positive rate (FPR) according to the available literature [31]. Based on these

230 parameters, we computed the ROC and the corresponding area under the curve (AUC) that can be

231 interpreted as follows:

232 AUC = 0.5 the test is not informative;

233 0.5 <AUC ≤0.7 the test is not accurate;

234 0.7 <AUC ≤0.9 the test is moderately accurate;

235 0.9 <AUC <1.0 the test is highly accurate;

236 AUC = 1 perfect test [32].

237 ROC analyses were performed using an in-house developed code in MATLAB (MATLAB and

238 Statistics Toolbox Release 2015b, The MathWorks, Inc., Natick, Massachusetts, USA).

239

240

Results

241

242

Conventional MRI vs MR Relaxometry

244 First, the conventional MR protocol was tested to identify the induced lesions. Based on T1w images,

245 a board-certified radiologist judged the lesion as 'not visible' in 46% of the subjects and 'barely

246 visible' in the remaining 54%. As an example, in Figs 3-5A the T1w images of three representative

247 patients are shown. It can be noted that with that the typical settings of T1w sequences, the induced

248 hemorrhages were not clearly identifiable in two of the reported cases (Figs 3 and 4A), while it was

249 barely visible in the last one (Fig 5A). The visualization of the lesions improved when T2w images

250 were considered (Fig 3-5B): the rate of lesions classified as 'not visible' dropped to 23% while the

251 proportion of 'clearly visible' and 'barely visible' raised to 39% and 38%, respectively (see Figs 3-

252 5B - white arrows). As it can be seen in the reported examples, lesions were characterized by ill-

253 defined patterns whose extension varied throughout the sample. In 22% of the sample, the lesions

11

254 were localized in the left frontal lobe (Fig 4), and in the remaining 78%, the lesions were localized in

255 the left thalamus (Figs 3 and 5).

256 Then, the T1 and T2 maps were estimated. In this case, a further improvement was obtained in terms

257 of lesion identification: lesions were judged as 'clearly visible' in most of the sample, namely 85%

258 for T1 maps (see Figs 3-5C) and 93% for T2 maps (see Figs 3-5D). In the remaining 5% and 7% for

259 T1 and T2 maps respectively the lesion was not clearly detectable. In general, as it can be seen in

260 Figs 3-5CD (white arrows), hyperintense lesions were observed with punctiform, linear, or irregular

261 shape whose size varied across subjects.

262 Eventually, hierarchical clustering was performed to classify brain tissues. As described in Section

263 2, a set of candidate voxels were selected based on T2 maps. As an example, we report in S1 Fig (see

264 supplementary material) voxels selected (black dots) and their homologous ones (red dots) for the

265 data of Fig 3. Based on their T1-relaxation signals (see S1B Fig), the hierarchical clustering was run.

266 The final classification of healthy (H-yellow) and pathological (P-red) voxels is reported in Figs 3-

267 5E overlaid on the T2 map (grayscale). Interestingly, in all reported cases, within the initially selected

268 area, the hierarchical clustering identified a subset of 'pathological' voxels. Theoretically, since

269 lesions were induced only in the left hemisphere, members of the P class were not expected in the

270 right hemisphere. This applied to the reported cases of Figs 3-5.

271

272 **Fig 3. Standard vs MRR analyses and histopathological validation. Example 1.**

273   A) T1w transverse image of the brain; the lesion has been classified as 'not visible'.

274   B) T2w transverse image of the brain; the lesion appears ill-defined, hyperintense, and linearly

275   shaped in the left thalamus (white arrow).

276   C-D) T1 and T2 maps, respectively. A hyperintense linearly shaped area is visible in both maps

277   (white arrow).

278   E) The output of the hierarchical cluster overlaid on the T2 map. Voxels classified as

279   "pathological" and "healthy" parenchyma are reported in red and yellow, respectively.

12

280 F) The results of gross anatomy. From the photograph of the brain section, the contour of the

281 hemorrhagic lesion characterized by a linear shape that mainly involves the left thalamus (white

282 arrow) has been delineated (white dotted line).

283 G) Histopathology results. The overall brain section obtained from the microscope with the

284 hemorrhagic lesion shown in greater detail superimposed on the overall section.

285 H) The MRR classification compared to both gross anatomy and histopathology: voxels

286 classified as pathological (red) fall inside the estimated true lesion contour.

287

288 **Fig 4. Standard vs MRR analyses and histopathological validation. Example 2.**

289 A) T1w transverse image of the brain; the lesion has been judged 'not visible' by a board

290 certified.

291 B) T2w transverse image of the brain. Also in this case the lesion appears ill-defined,

292 hyperintense and linearly shaped in the left thalamus (white arrow)

293 C-D) T1 and T2 maps, respectively. A hyperintense linear-shaped area is visible in both maps

294 (white arrow).

295 E) The output of the hierarchical cluster overlaid on the T2 map. Voxels classified as

296 "pathological" and "healthy" parenchyma are reported in red and yellow, respectively.

297 F) The results of gross anatomy. From the photograph of the brain section, the contour of the

298 hemorrhagic lesion characterized by a linear shape that involves the left frontal lobe (white

299 arrow) has been delineated (white dotted line).

300 G) Histopathology results. The overall brain section obtained from the microscope with the

301 hemorrhagic lesion shown in greater detail superimposed on the overall section is reported.

302 H) A good agreement can be noted between the MRR classification and the lesion contour

303 estimated from both gross anatomy and histopathology.

304

305

13

306

Fig 5. Standard vs MRR analyses and histopathological validation. Example 3.

A) T1w transverse image of the brain; the lesion appears ill defined, hypointense, and irregular in the left thalamus (white arrow).

B) T2w transverse image of the brain. As in T1w, the lesion in the left thalamus appears ill-defined, irregular but hyperintense (white arrow).

C-D) T1 and T2 maps, respectively. A hyperintense and irregularly shaped area is visible in both maps (white arrow).

E) The output of the hierarchical cluster overlaid on the T2 map. Voxels classified as "pathological" and "healthy" parenchyma are reported in red and yellow, respectively.

F) The results of gross anatomy. From the photograph of the brain section, the contour of the hemorrhagic lesion that appears irregular in shape and involves the left thalamus (white arrow) has been delineated (white dotted line).

G) Histopathology results. The overall brain section obtained from the microscope with the hemorrhagic lesion shown in greater detail superimposed on the overall section.

H) The hemorrhagic lesion found by the MRR approach (red voxels) is in agreement with the gross anatomy: voxels classified as pathological fall inside the true lesion contour. It can be noted that in panel F) the hemorrhagic area appears more extended than the lesion histologically evident (G). However, this can be due to postmortem blood spread in the space between the left hemisphere and the ipsilateral thalamus. The contour of the hyperintense area in both T1 and T2 maps is in very good agreement with the hemorrhagic area evident from the histopathological results where the blood spread disappeared after the formalin fixation.

However, there have been cases where classification partially failed and labeled as pathological also voxels in the healthy hemisphere, see for example Fig 6.

332

333 **Fig 6. Misclassification results**

334 A, D) The results of MRR classification do not show a clear distinction between the two groups of

335 pathological vs healthy parenchyma, since pathological tissue was found in the healthy hemisphere.

336 B, E) The hemorrhagic lesion contour (white dashed line) estimated from the gross anatomy.

337 C-F) The comparison between the MRR classification and the true lesion contour shows that in these

338 two cases the performance of the classifier is poor since both healthy (yellow) and pathological (red)

339 voxels fall inside the lesion contour.

340

341

342

343 This aspect may be justified due to blood heparinization that may have led to a lack of a clear division

344 between the hemorrhage and the brain parenchyma, see Discussion.

345 These findings show that it is fundamental to validate accurately the proposed approach. To this aim,

346 we assessed the classification performance by comparing these results with the histopathological

347 assessment.

348

Histopathology assessment

349

350 The induced hemorrhages varied in size and shape, and a superficial, subdural, or subarachnoid

351 collection of blood was also usually observed. Most frequently affected areas were represented by

352 the frontal cerebral cortex (gray and white matter), cingulate gyrus, and caudate nucleus.

353 Histologic evaluation was performed to identify the pattern of hemorrhage and perihaemorrhage

354 tissue changes. Serial sections allowed to observe the extension of the hemorrhagic area caused by

355 the needle-induced direct trauma and the aspect of perilesional tissues, not affected by the blood

356 accumulation. In all the brains, a hemorrhagic lesion was detected with a pattern characterized by a

357 moderate variation of intensity from case to case (Fig 7). The injected blood caused disruption of the

15

358   surrounding neural tissue, termed mass effect (Fig 7A, B) Fragmented nuclear debris was observed

359   in damaged perihematomal tissue, in association with the presence of perihematomal edema,

360   frequently characterized by gray matter vacuolization, neuronal perinuclear halos (Fig. 7C black

361   arrow; 7D black arrow), and multifocal, mild dilation of perivascular (Virchow-Robin) spaces. Red

362   blood cells within the wall of small vessels (intramural erythrocytes) and scattered swollen

363   endothelial cells were also seen (Fig 7D white arrow). Also, multifocal cell shrinkage, with the

364   presence of scattered hypoxic-ischemic neurons was detected in almost all cases (Fig 7D arrowhead;

365   7E arrow). For comparison, neural tissues distant from the hematoma in the same section, as well as

366   the corresponding contralateral areas in the unaffected cerebral hemisphere were examined, and no

367   significant alterations were recorded, thus allowing to exclude the occurrence of histologic artifacts

368   due to brain fixation or manipulation (Fig 7F).

369

370   **Fig 7. Histopathological sections**

371   A-B) Low (A) and high (B) magnification of brain sections passing through the needle path, showing

372   a linear hemorrhagic area.

373   C-D) Histological images of peri-hemorrhage neural tissue, showing variably intense, (C) gray

374   (perinuclear halos; arrow) and (D) white matter edema (black arrow) and multifocal neuronal

375   shrinkage (arrowhead). Red blood cells within the wall of a small vessel are also visible (white arrow).

376   E) Higher magnification of multifocal neuronal shrinkage (arrows) in peri-hemorrhagic tissue.

377   F) Histologically normal neurons in the contralateral area of the unaffected cerebral hemisphere.

378

379   The above aspects evidence the structural difference between the brain hemisphere with induced

380   hemorrhage and the healthy one, thus confirming that the hyperintense areas on T1 and T2 maps were

381   not artifactual in nature and correspond to real lesions.

382

383

384

385

Validation of the proposed approach

387   To validate the proposed approach, we compared, through a ROC analysis, the MRR results with the

388   histopathological ones described above. For every patient, the lesion contours were manually

389   delineated from both gross anatomy and histopathological images. In Figs 3-5F, we show the lesion

390   contour (dashed line) extracted from a photograph of the section of the brain immediately after the

391   extraction, typically within 10-15 minutes after the end of the MRI session. This section was selected

392   as explained in Section 2, to match the MRI transverse plane where the relaxometry study was

393   performed. Furthermore, the lesion contour was also obtained from the gross anatomy sections and

394   microscopic analyses performed at 48 hours after the brain was kept in formalin. The macroscopic

395   image of the brain section with an inset from the microscopic analyses of the hemorrhages is reported

396   in Figs 3-5G. As it can be noted in Figs 3-5H, where the classification and anatomy results are

397   superimposed, a good agreement between the gross anatomy (dashed) and MRR classified voxels

398   (red) was obtained. However, as far as it regards the cases shown in Fig 6, the classification seems to

399   match only the initial part of the lesion (see Fig 6C) or half of it (Fig 6F). Now, to quantitatively

400   validate the MRR approach, (see Section 2) the TPR and FPR for each lesion were computed. The

401   results reported in Table 2 seem promising since the mean TPR was 0.76, the mean FPR was 0.13

402   leading to an overall accuracy of 0.83.

403

404

405

406

407

408

409

410

411

412   **Table 2. ROC analyses**.

RABBIT	TRUE POSITIVE RATE (TPR)	FALSE POSITIVE RATE (FPR)	ACCURACY
1	0.87	0.34	0.77
2	0.62	0.18	0.74
3	1	0	1
4	0.7	0.3	0.7
5	0.67	0.05	0.89
6	0.67	0.2	0.74
7	1	0.15	0.92
8	0.34	0	0.67
9	1	0	1
10	0.95	0.17	0.88
11	1	0	1
12	0.3	0	0.65
13	0.91	0	0.96
MEAN	**0.76**	**0.12**	**0.83**

413

414   TPR, FPR, and accuracy are reported for each rabbit.

415

416   In Fig 8 the ROC curve is reported (the point 1 and 0 are reported only for clarity purpose to show to

417   reference bisecting line). As it can be noted, the classification performance is well beyond the chance

18

418 (0.5, dashed line) level, being the area under the curve AUC = 0.87. This value, compared to the

419 thresholds reported in Section 2, places the performance of the classification close to the edge of

420 "highly accurate" level (AUC = 0.9).

421

422

423 **Fig 8. ROC analysis**

424 The ROC curve shows that the classifier performance (black line) is beyond the chance level (red

425 line). The area under the curve (AUC=0.87) compared to the thresholds reported in Section 2, places

426 the performance of the classification close to the "highly accurate" level (AUC = 0.9).

427

428

Discussion

430

431 In this study, we proposed a multivariate MRR approach to identify subtle brain hemorrhages on a

432 rabbit model. The developed technique, which supports a diagnosis at the subject level, has been

433 compared to conventional MRI and validated through histopathological examinations. The proposed

434 approach, being optimized for a low field scanner, routinely available in the veterinary facilities, has

435 the advantage of a potential direct translation into the clinical practice.

436 In general, the MRI sensitivity for detecting subtle lesions such as edema or hemorrhages increases

437 with the magnetic field. Thus, with low field scanners typically used in veterinary practice, these

438 hemorrhagic diseases are likely to be underdiagnosed [25]. For this reason, we tested our approach

439 on induced hemorrhagic lesions obtained by injecting a minimal amount of blood to create a

440 reproducible and lateralized lesion. This allowed to compare the injured and healthy parenchyma

441 within a single MR scan. This approach is in line with previous works in the literature, for example

442 in [33] the authors injected autologous blood in the right hemisphere of rat brains to evaluate the

19

443 effects of experimental intracerebral hemorrhage on brain tissue injury and recovery. They reported

444 that MR relaxometry can be promising to observe the lesion progression. Our choice to focus on T1

445 and T2 Relaxometry, instead of T2*, shown also reliable in visualizing hemorrhage [34], is also in

446 line with previous MRR studies on this kind of lesions [22,26,33]. In fact, to setup T2* relaxometry

447 protocols can be very challenging with a low field clinical scanner, and thus T1/T2 MRR has the

448 advantage of being more easily implemented in the future by veterinary practitioners on a large scale.

449 The proposed approach is multivariate, i.e. it combined both T1 and T2 information: the highest

450 contrast in the T2 map was exploited to select the initial ROIs, while the hierarchical clustering was

451 driven by the T1-based signal recovery. In fact, in terms of qualitative evaluation, in our data, the

452 lesions resulted always more evident in T2 maps than in T1 ones. Moreover, the adoption of the T1

453 signal to drive the classification is in line with the literature where T1 relaxometry has been proved

454 to be useful to assess brain parenchyma even with low filed scanners [22,35]. Nevertheless, this

455 choice leads to a higher acquisition time, which is one of the main drawbacks of the proposed

456 approach. Previous works showed that at higher magnetic fields (>0.25 T) T2* MRR can alleviate

457 this aspect and reliably identify brain hemorrhages, see for example [34].

458 The adoption of hierarchical clustering in this study, is supported by the fact that this approach has

459 been previously applied in the histopathological field to distinguish different tissue features, see for

460 example [36–38] and lesions characterized by different patterns [39–41]. In the case of subtle lesions,

461 such identification with standard MRI techniques can be very and any advanced analysis tool must

462 be validated. To this aim, here, the classification performance was directly addressed through the

463 comparison with histopathological analyses.

464 As far as it strictly concerns the histopathology findings, in acute human spontaneous intracerebral

465 hemorrhages, as well as in those induced by injecting blood in different animal models (42), primary

466 tissue damage is followed by secondary pathological lesions, in which cellular and

467 neuroinflammatory changes are poorly defined. Most of the studies published on this topic refer to

468 24/48 hours postmortem histological changes [43,44], especially focusing on the time and mass effect

20

469   of the lesion, cerebral edema, and ischemic cell changes affecting the adjacent neural tissue.

470   Consistently, in all our cases the histopathological examination on fixed tissue, one hour after

471   suppression, showed initial alterations such as peri-hemorrhage edema as well as mild vascular and

472   neuronal degeneration. The findings were crucial to confirm our MR tissue classification. In fact, the

473   lesion contours extracted using the gross anatomy and histopathological images showed a good

474   performance of the MRR classification.

475   However, in some cases, the adopted approach partially failed to identify the lesion. This could be to

476   a small amount of blood that, because of heparinization, slightly infiltrated the neural tissues around

477   the line of needle insertion during the injection. Such a small blood infiltration in the surrounding

478   healthy parenchyma could make the MRR clustering unable to distinguish the boundary real

479   hemorrhage-healthy tissues that instead appears evident from the histopathology after the brain

480   fixation. This hypothesis related to heparinization is supported by the work of Dai et al. (2018), where

481   authors, contrary to what has been herein described, used autologous nonheparinized blood into

482   cerebral parenchyma for their experiment and observed in their results a clear distinction between

483   hemorrhagic tissue and parenchyma [42].

484   In general, caution must be taken in comparing the histopathological and MRI analyses, for several

485   reasons, e.g different slice thickness on MRI images and gross anatomy, potential misalignment, the

486   effect of formalin fixation. Specifically, it has been reported that there is a reduction in tissue volume

487   of approximately 33% after formalin fixation and paraffin embedding [45]. This may have influenced

488   the data comparison, since after tissue fixation the size of the original lesion investigated with

489   relaxometry may have changed, thus relying on a possible bias during results data co-registration and

490   agreement quantification. Nevertheless, the obtained sensitivity and specificity place the classifier at

491   the edge between moderate and highly accurate.

492   The current results pave the way for future Artificial Intelligence (AI) based techniques which are

493   being developed to assist physicians in improving their diagnosis [46]. In this scenario, after being

494   trained, a classification algorithm automatically maps the observations to a set of classes. Our work

495 can be considered seminal for future AI applications validating a combined T1/T2 MRR hierarchical

496 clustering for the classification step [47,48]. At the current stage, in our approach, the training is

497 missing, and the proposed procedure is semi-automatic relying on a manual selection of candidate

498 ROIs. However, the algorithm training requires datasets whose size is larger than our current sample.

499 Therefore, it represents a future development of this technique where part of the data will train the

500 classifier, and the remaining will be automatically classified [49,50].

501 To conclude, to the best of our knowledge, this is the first report on an advanced MRR classification

502 tested on a routinely low field scanner showing that MRI diagnostic potential could be improved

503 especially in animal brain disorders causing subtle lesions (such as e.g distemper encephalitis or

504 hepatic encephalopathy).

505

506

507

508 # Acknowledgments

511

512

513

514

515

516

517

518

519

520

References

521

522

523   1.   Robertson I. Optimal Magnetic Resonance Imaging of the Brain. Vet Radiol Ultrasound.

524   2011;52(s1):S15–22.

525   2.   Thrall DE. Magnetic Resonance Imaging Features of Disease. In: Small Animals in

526   Textbook of Veterinary Diagnostic Radiology.7th Ed. Elsevier; 2018. p. 204.

527   3.   Cheng H-LM, Stikov N, Ghugre NR, Wright GA. Practical medical applications of

528   quantitative MR relaxometry. J Magn Reson Imaging. 2012;36(4):805–24.

529   4.   Deoni SCL. Quantitative Relaxometry of the Brain. Top Magn Reson Imaging.

530   2010;21(2):101–13.

531   5.   de Blank P, Badve C, Gold DR, Stearns D, Sunshine J, Dastmalchian S, et al. Magnetic

532   Resonance Fingerprinting to Characterize Childhood and Young Adult Brain Tumors. Pediatr

533   Neurosurg. 2019;54(5):310–8.

534   6.   Fathi Kazerooni A, Nabil M, Zeinali Zadeh M, Firouznia K, Azmoudeh-Ardalan F, Frangi

535   AF, et al. Characterization of active and infiltrative tumorous subregions from normal tissue in

536   brain gliomas using multiparametric MRI. J Magn Reson Imaging. 2018;48(4):938–50.

537   7.   Ellingson BM, Cloughesy TF, Lai A, Nghiemphu PL, Lalezari S, Zaw T, et al.

538   Quantification of edema reduction using differential quantitative T2 (DQT2) relaxometry mapping

539   in recurrent glioblastoma treated with bevacizumab. J Neurooncol. 2012;106(1):111–9.

540   8.   Hattingen E, Jurcoane A, Daneshvar K, Pilatus U, Mittelbronn M, Steinbach JP, et al.

541   Quantitative T2 mapping of recurrent glioblastoma under bevacizumab improves monitoring for

542   non-enhancing tumor progression and predicts overall survival. Neuro-Oncol. 2013;15(10):1395–

543   404.

544   9.   Lescher S, Jurcoane A, Veit A, Bähr O, Deichmann R, Hattingen E. Quantitative T1 and T2

545   mapping in recurrent glioblastomas under bevacizumab: earlier detection of tumor progression

546   compared to conventional MRI. Neuroradiology. 2015;57(1):11–20.

547   10.   Chen H, Yu G, Wang J, Li F, Li G. Application of T2 relaxometry in lateralization and

548   localization of mesial temporal lobe epilepsy and corresponding comparison with MR volumetry.

549   Acta Radiol Stockh Swed 1987. 2016;57(9):1107–13.

550   11.   Goubran M, Hammond RR, de Ribaupierre S, Burneo JG, Mirsattari S, Steven DA, et al.

551   Magnetic resonance imaging and histology correlation in the neocortex in temporal lobe epilepsy.

552   Ann Neurol. 2015;77(2):237–50.

553   12.   Khan AR, Goubran M, de Ribaupierre S, Hammond RR, Burneo JG, Parrent AG, et al.

554   Quantitative relaxometry and diffusion MRI for lateralization in MTS and non-MTS temporal lobe

555   epilepsy. Epilepsy Res. 2014;108(3):506–16.

556   13.   Coan AC, Bonilha L, Morgan PS, Cendes F, Li LM. T2-weighted and T2 relaxometry

557   images in patients with medial temporal lobe epilepsy. J Neuroimaging. 2006;16(3):260–5.

558   14.   Vos SB, Winston GP, Goodkin O, Pemberton HG, Barkhof F, Prados F, et al. Hippocampal

559   profiling: Localized magnetic resonance imaging volumetry and T2 relaxometry for hippocampal

560   sclerosis. Epilepsia. 2020;61(2):297–309.

561   15.   Winston GP, Vos SB, Burdett JL, Cardoso MJ, Ourselin S, Duncan JS. Automated T2

562   relaxometry of the hippocampus for temporal lobe epilepsy. Epilepsia. 2017;58(9):1645–52.

563   16.   Gracien R-M, Reitz SC, Hof S-M, Fleischer V, Zimmermann H, Droby A, et al. Assessment

564   of cortical damage in early multiple sclerosis with quantitative T2 relaxometry. NMR Biomed.

565   2016;29(4):444–50.

566   17.   Lönnfors-Weitzel T, Weitzel T, Slotboom J, Kiefer C, Pollo C, Schüpbach M, et al. T2-

567   relaxometry predicts outcome of DBS in idiopathic Parkinson's disease. NeuroImage Clin. 1

568   2016;12:832–7.

569   18.   Knight MJ, Wearn A, Coulthard E, Kauppinen RA. T2 Relaxometry and Diffusion Tensor

570   Indices of the Hippocampus and Entorhinal Cortex Improve Sensitivity and Specificity of MRI to

571   Detect Amnestic Mild Cognitive Impairment and Alzheimer's Disease Dementia. J Magn Reson

24

572 Imaging. 2019;49(2):445–55.

573 19.   Deruelle T, Kober F, Perles-Barbacaru A, Delzescaux T, Noblet V, Barbier EL, et al. A

574 Multicenter Preclinical MRI Study: Definition of Rat Brain Relaxometry Reference Maps. Front

575 Neuroinformatics 2020; 14: 22.

576 20.   Sénégas J, Liu W, Dahnke H, Song H, Jordan EK, Frank JA. Fast T2 relaxometry with an

577 accelerated multi-echo spin-echo sequence. NMR Biomed. 2010;23(8):958–67.

578 21.   Lorincz BA, Anson A, Csébi P, Bajzik G, Biró G, Tichy A, et al. Novel approach to

579 magnetic resonance imaging of epileptic dogs - T2 relaxometry of the brain with emphasised

580 hippocampus. Acta Vet Hung. 2017;65(2):185–97.

581 22.   Del Signore F, Vignoli M, Marruchella G, Simeoni F, Tamburro R, Aste G, et al. The

582 potential role of magnetic resonance brain relaxometry in veterinary medicine: a preliminary study.

583 J Biol Regul Homeost Agents. 2019;33(6):1725–36.

584 23.   Konar M, Lang J. Pros and cons of low-field magnetic resonance imaging in veterinary

585 practice. Vet Radiol Ultrasound. 2011;52(1 Suppl 1):S5–14.

586 24.   Rusbridge C, Long S, Jovanovik J, Milne M, Berendt M, Bhatti SFM, et al. International

587 Veterinary Epilepsy Task Force recommendations for a veterinary epilepsy-specific MRI protocol.

588 BMC Vet Res. 2015;11:194.

589 25.   Mai W. Brain Hemorrhage. In: Diagnostic MRI in Dogs and Cats. 1st Ed. CRC Press; 2018.

590 p. 284

591 26.   Pan W, Yan Q, Qin M, Jin G, Sun J, Ning X, et al. Detection of Cerebral Hemorrhage in

592 Rabbits by Time-Difference Magnetic Inductive Phase Shift Spectroscopy. PLoS ONE. 2015

593 .22;10(5):e0128127.

594 27.   Huhdanpaa H, Hwang DH, Gasparian GG, Booker MT, Cen Y, Lerner A, et al. Image

595 coregistration: quantitative processing framework for the assessment of brain lesions. J Digit

596 Imaging. 2014;27(3):369–79.

597 28.   Lagarias JC, Reeds JA, Wright MH, Wright PE. Convergence Properties of the Nelder-

598   Mead Simplex Method in Low Dimensions. SIAM J Optim. 1998;9:112–47.

599   29.   Carneiro A a. O, Vilela GR, Araujo DB de, Baffa O. MRI relaxometry: methods and

600   applications. Braz J Phys. 2006;36(1A):9–15.

601   30.   Rousseeuw PJ. Silhouettes: A graphical aid to the interpretation and validation of cluster

602   analysis. J Comput Appl Math. 1987;20:53–65.

603   31.   Altman DG, Bland JM. Diagnostic tests. 1: Sensitivity and specificity. BMJ.

604   1994;308(6943):1552.

605   32.   D'Arrigo G, Provenzano F, Torino C, Zoccali C, Tripepi G. [Diagnostic tests and ROC

606   curves analysis]. G Ital Nefrol. 2011;28:642–7.

607   33.   Knight Robert A., Han Yuxia, Nagaraja Tavarekere N., Whitton Polly, Ding Jennifer,

608   Chopp Michael, et al. Temporal MRI Assessment of Intracerebral Hemorrhage in Rats. Stroke.

609   2008;39(9):2596–602.

610   34.   Küker W, Thiex R, Rohde I, Rohde V, Thron A. Experimental acute intracerebral

611   hemorrhage. Value of MR sequences for a safe diagnosis at 1.5 and 0.5 T. Acta Radiol Stockh

612   Swed 1987. 2000;41(6):544–52.

613   35.   Zotev VS, Matlashov AN, Savukov IM, Owens T, Volegov PL, Gomez JJ, et al. SQUID-

614   Based Microtesla MRI for In Vivo Relaxometry of the Human Brain. IEEE Trans Appl Supercond.

615   2009;19(3):823–6.

616   36.   Au NHC, Cheang M, Huntsman DG, Yorida E, Coldman A, Elliott WM, et al. Evaluation of

617   immunohistochemical markers in non-small cell lung cancer by unsupervised hierarchical

618   clustering analysis: a tissue microarray study of 284 cases and 18 markers. J Pathol. settembre

619   2004;204(1):101–9.

620   37.   Bunyak F, Hafiane A, Palaniappan K. Histopathology tissue segmentation by combining

621   fuzzy clustering with multiphase vector level sets. Adv Exp Med Biol. 2011;696:413–24.

622   38.   Fouad S, Randell D, Galton A, Mehanna H, Landini G. Unsupervised morphological

623   segmentation of tissue compartments in histopathological images. PloS One.

624   2017;12(11):e0188717.

625   39.   Wang Y, Li T-Q. Analysis of whole-brain resting-state FMRI data using hierarchical

626   clustering approach. PloS One. 2013;8(10):e76315.

627   40.   Cordes D, Haughton V, Carew JD, Arfanakis K, Maravilla K. Hierarchical clustering to

628   measure connectivity in fMRI resting-state data. Magn Reson Imaging. 2002;20(4):305–17.

629   41.   Gors D, Suetens P, Vandenberghe R, Claes P. Hierarchical spectral clustering of MRI for

630   global-to-local shape analysis: Applied to brain variations in Alzheimer's disease. In: 2017 IEEE

631   14th International Symposium on Biomedical Imaging (ISBI 2017). 2017. pag. 787–91.

632   42.   Dai M, Liu X-C, Li H-T, Xu C-H, Yang B, Wang H, et al. EIT Imaging of Intracranial

633   Hemorrhage in Rabbit Models Is Influenced by the Intactness of Cranium. BioMed Res Int.

634   2018;2018:1–10.

635   43.   Koeppen AH, Dickson AC, McEvoy JA. The cellular reactions to experimental intracerebral

636   hemorrhage. J Neurol Sci. 1995;134:102–12.

637   44.   Shtaya A, Bridges LR, Esiri MM, Lam-Wong J, Nicoll JAR, Boche D, et al. Rapid

638   neuroinflammatory changes in human acute intracerebral hemorrhage. Ann Clin Transl Neurol.

639   2019;6(8):1465–79.

640   45.   Bancroft J. Theory and practice of histological techniques. 5th Ed. Elsevier; p. 71–72.

641   46.   Topol E. High-performance medicine: the convergence of human and artificial intelligence.

642   Nat Med. 2019;25.

643   47.   Sulaiman SN, Non NA, Isa IS, Hamzah N. Segmentation of brain MRI image based on

644   clustering algorithm. In: 2014 IEEE Symposium on Industrial Electronics Applications (ISIEA).

645   2014. pag. 60–5.

646   48.   Saha S, Bandyopadhyay S. MR Brain Image Segmentation Using A Multi-seed Based

647   Automatic Clustering Technique. Fundam Informaticae. 2009;97(1–2):199–214.

648   49.   Arbabshirani MR, Plis S, Sui J, Calhoun VD. Single subject prediction of brain disorders in

649   neuroimaging: Promises and pitfalls. NeuroImage. 2017;145(Part B):137–65.

650   50.   Vabalas A, Gowen E, Poliakoff E, Casson AJ. Machine learning algorithm validation with a

651   limited sample size. PLoS ONE. 2019. 7;14(11):e0224365

652

Supporting Information

S1 Fig Analysis pipeline

A) The voxels manually selected on the suspected lesion (black dots) are automatically extracted on the contralateral hemisphere (red dots) based on the brain midline. This step is based on the T2 map.

B) T1 based signals are extracted from the selected set of voxels. These patterns will be input to the hierarchical classification.

C) The final dendrogram for the data is pointed, and it can be seen that the cluster silhouette suggested that optimal separation corresponded to two clusters respectively healthy and hemorrhagic tissue.

D) The classifier is validated through the histopathological results. The validation is based on the true lesion contour and quantified employing ROC parameters such as TPR, FPR, and accuracy.
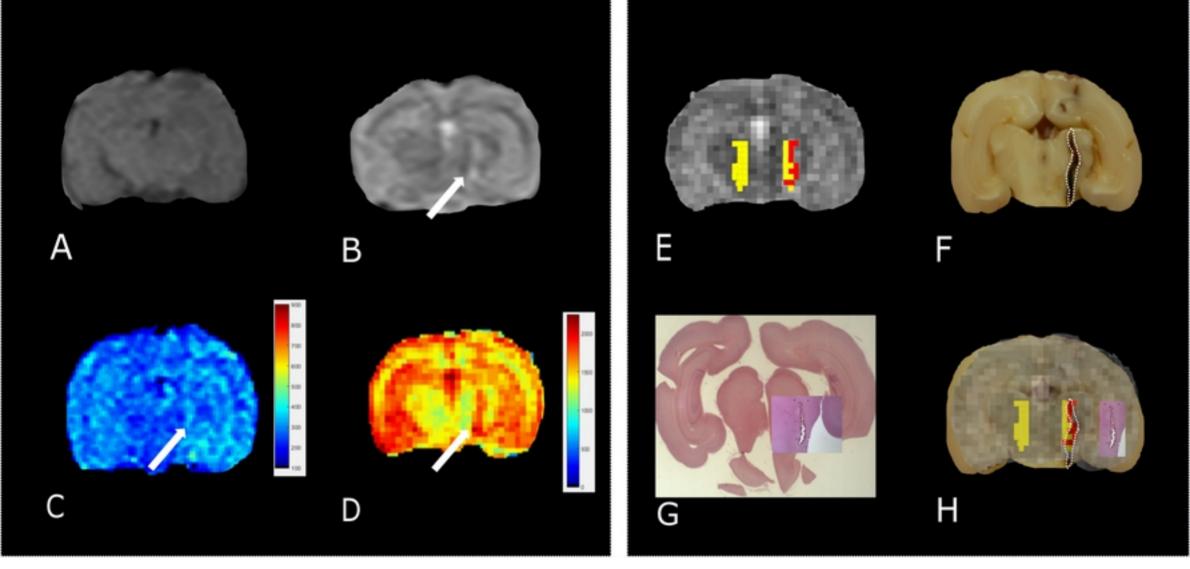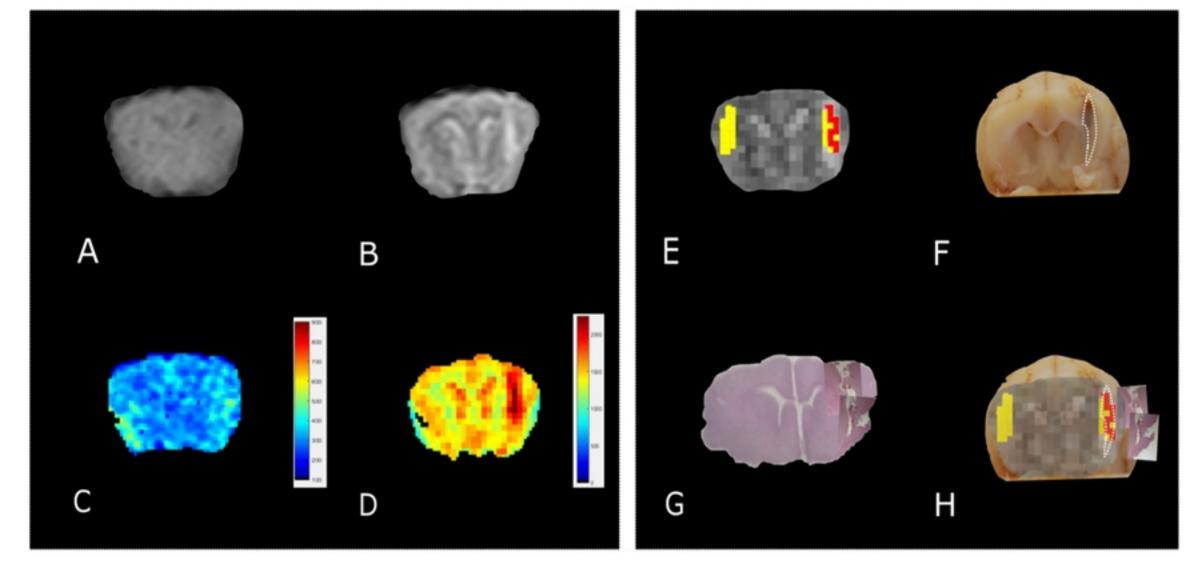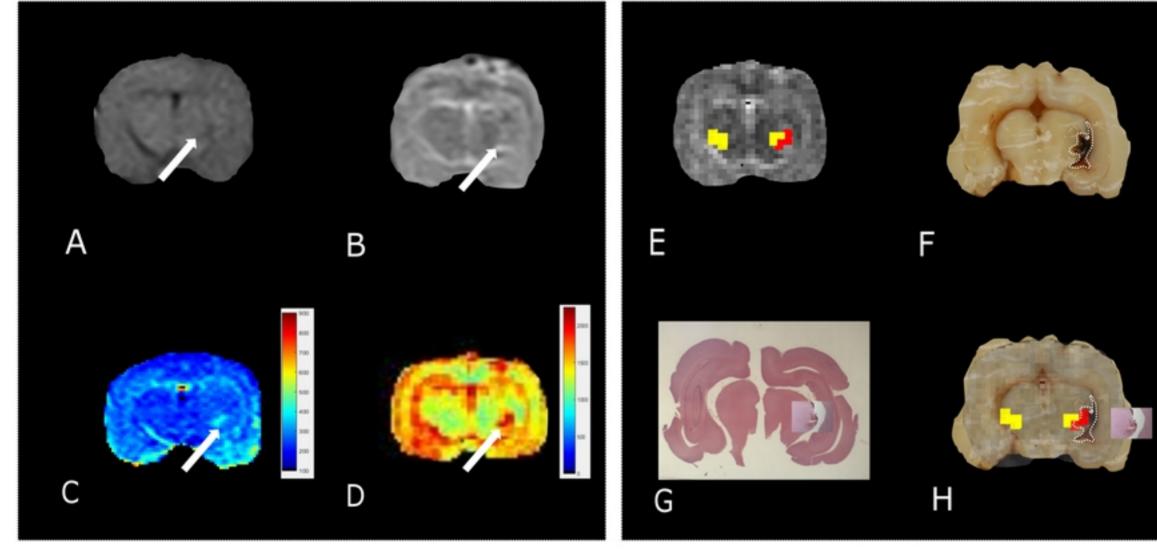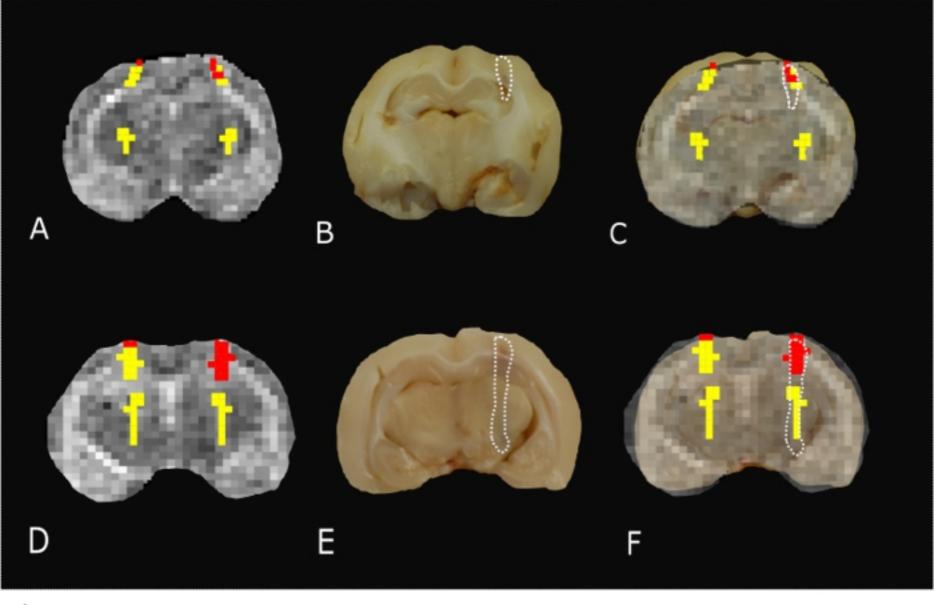
Figure 1

Figure 2

Figure 3

Figure 4

Figure 5

Figure 6

Figure 7

Figure 8